OPPORTUNISTIC SPACE-BASED ORBIT DETERMINATION OF RESIDENT SPACE OBJECTS USING THE TUBIN SPACECRAFT

Victoria Koßack*, Vincent Schulz*, Anton Große Siestrup*, Johanna E. C. Teuchert*, Clément Jonglez, Elizabeth Klioner, and Enrico Stoll

Chair of Space Technology, Marchstraße 12-14, 10587 Berlin, Germany
Email: {v.kossack, v.schulz, a.grosse.siestrup, j.teuchert}@tu-berlin.de
** Contributed equally*

ABSTRACT

The growing number of resident space objects around Earth poses significant risks to spacecraft operations and space infrastructure. Addressing this requires accurate orbit determination for objects of all sizes. Reliable tracking of smaller objects requires robust space-based orbit determination, which is being developed as part of the proposed PRecise IN-orbit Collision prediction and space Environment Surveillance System (PRINCESS) mission. During a close encounter, the Technische Universität Berlin Infrared Nanosatellite (TUBIN) spacecraft has captured visual and infrared images of a passing spacecraft, offering a unique opportunity to perform space-based orbit determination based on real-world observations. This paper studies the feasibility and achievable accuracy of such an approach, using a Gauss angles-only method in combination with the Herrick-Gibbs method. The challenges and lessons learned are laid out to aid in the design and operations of future space-based orbit determination missions, like PRINCESS, and similar opportunities.

Keywords: Space-Based Orbit Determination; Space-Debris; TUBIN; PRINCESS; Education.

1. INTRODUCTION

As the number of objects orbiting Earth grows, stringent monitoring of the space environment is required to ensure the safety of space-based infrastructure. Ground-based observations using radar can only reliably track objects larger than $10\,\mathrm{cm}$ [1]. To address these shortcomings, space agencies and commercial companies are researching space-based orbit determination. In May 2024, TU Berlin's satellite Technische Universität Berlin Infrared Nanosatellite (TUBIN) [1] had a close encounter with the satellite ICEYE-12 (ICEYE), during which a number of images of the passing satellite have been captured by TUBIN's visible spectrum (VIS) and Infra-Red (IR) cameras. As space-based orbit determination becomes increasingly important in the context of the steadily overpopulating Low Earth Orbit (LEO), these images offer a valuable opportunity to analyze the capability of space-based orbit determination with passive optical instruments somewhat similar to the conditions expected during the proposed Technische Universität Berlin (TU Berlin) mission PRecise IN-orbit Collision prediction and space Environment Surveillance System (PRINCESS) [2].

It is important to note that this paper is written by a group of students following the TU Berlin lecture ”Space Mission Analysis” building on an existing MATLAB code base written by the students over a semester. Therefore, the goal of this paper is not to gain the best possible Initial Orbit Determination (IOD) result but to gauge the achievable accuracy with the rather basic methods implemented during this lecture as well as to identify challenges that occur when using space-based observation data. In particular, this paper is limited to using the Gauss Angles-Only (GAO) approach in combination with Gibbs and Herrick-Gibbs method as presented in [3]. Nevertheless, this close encounter poses a valuable opportunity to evaluate the method's accuracy for space-based observations and gain valuable insights into the challenges of space-based orbit determination under real-life conditions, providing numerous lessons learned for further observation campaigns or dedicated missions like PRINCESS.

The TUBIN spacecraft encompasses three cameras, one of them recording in the VIS spectrum, and two of them in the IR spectrum, increasing the number of pictures and therefore observation points. The VIS camera has captured the passing spacecraft with an exposure time of $0.1\,\mathrm{s}$, which results in a motion-blurred picture, in which the passing satellite can be seen as an elongated light strip. Figure 1 shows an overlay of all eight VIS images. The initial and final point of the light line can be utilized as two separate observation points, one at the beginning of exposure and the other at the end. Following the angle determination in each picture, coordinate transformations accounting for mounting angles of the cam-

[1] https://www.tu.berlin/raumfahrttechnik/forschung/aktuelle-projekte/tubin

Proc. 9th European Conference on Space Debris, Bonn, Germany, 1–4 April 2025, published by the ESA Space Debris Office
Editors: S. Lemmens, T. Flohrer & F. Schmitz, (http://conference.sdo.esoc.esa.int, April 2025)

Figure 1. Overlay of All Eight Captured VIS Images with Annotation of the Observation Points

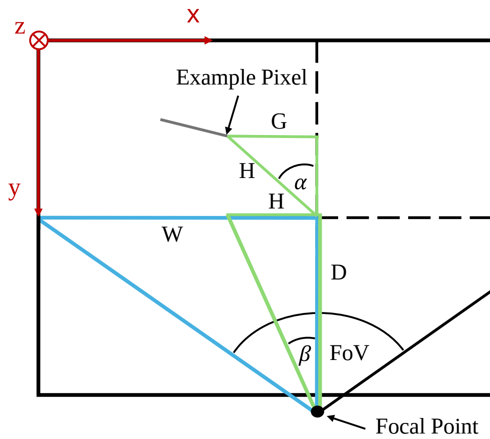

Figure 2. Visualization of Azimuth and Elevation Determination

eras themselves and attitude and data of TUBIN at the time of the observations the orbit determination approach called GAO is implemented. Across the three cameras, 24 images have been taken from which 32 observation points can be generated.

This paper covers the entire process from extracting the angular observations from the images through coordinate transformation, slant range estimation to orbit determination of the passing satellite. The determined orbit is compared to the orbit described by the two-line element (TLE) valid at the time of the encounter. An accuracy analysis of the selected method and an analysis of measurement and installation errors are performed to estimate the applicability on future missions, like the PRINCESS mission.

2. OBSERVATION ANGLE DETERMINATION

Based on the captured images (Figure 1), observation angles are determined, which is described below in Section 2.1. As the GAO approach is used as the initial orbit determination method, azimuth and elevation must be transformed into the Earth-centered inertial (ECI) coordinate system. This transformation is elaborated in Section 2.2

2.1. Determination of Angles in the Camera Frame

The observation angles are first calculated in the respective camera-fixed frame. Two angles are determined: an azimuth angle and an elevation angle. The observation angle determination described in this section is implemented in Python. The image processing is based on a method called the MEHthod [4], which determines the Moon and Earth horizon in an image and calculates the spacecraft's attitude with the imagery. In this script, the image is converted into black and white so that the pixel stripes that represent the foreign spacecraft are depicted in white and space is represented in black. Like in the MEHthod, a threshold is used which determines whether a pixel shall be part of the spacecraft stripe. This allows to use only bright spacecraft pixels for angle determination. For VIS images, the distance to the most left pixel of the spacecraft stripe and to the most right pixel is calculated from the center of the image. One VIS image gives two pairs of angles in the camera frame: one for the most left pixel and one for the most right pixel of the stripe. These pixels are the observation points of the image. In between, the foreign spacecraft moved with a duration of the exposure time. For IR images only the pixel in the middle of the spacecraft stripe is analyzed due to the lower resolution of the IR cameras. The azimuth is calculated by spanning a triangle as seen in Figure 2 as the upper green triangle. This visualization in Figure 2 is done for an example pixel. However, the same is done for all identified observation pixels of all images. With this trigonometric relation, the azimuth α is determined with

$$\alpha = arcsin\left(\frac{G}{H}\right) \tag{1}$$

where G is the distance from the center to the pixel in the y-direction and H is the normed distance from the center to the pixel. Both are determined in pixel units. This angle is then offset with 270° because the azimuth should start at the upper mid of the image.

The elevation angle in the camera frame is determined with two other trigonometric relations, which can be seen in Figure 2 as well. In this case, a triangle is spanned in the third dimension, in this case the z-direction of the image. This blue triangle is spanned between the left side of the image, the middle of the image in the x-direction and the focal point. From this point, the field of view (FoV) of the camera is defined. This FoV is used to calculate the distance D from the focal point to the middle of the image with

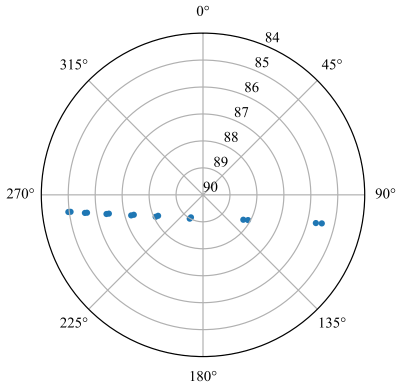

Figure 3. Polar Plot of Azimuth and Elevation for all Observation Points

$$D = \frac{W}{tan\left(\frac{FoV}{2}\right)} \tag{2}$$

where W corresponds to half of the image size in x direction. With the distance D, another triangle is spanned, which includes the distance H from the azimuth calculation, the distance D and the elevation angle β. With this triangle, the elevation angle β in the image frame is calculated with

$$\beta = arctan\left(\frac{H}{D}\right) \tag{3}$$

All calculations are done using pixel units. The angles are calculated in radians and are output as degrees for visualization in the plots.

Since there is no appropriate method to verify the determined observation angles, a polar plot of the determined angles is presented in Figure 3. Comparing this polar plot with the overlay of visual images taken during the close approach in Figure 1, the movement in the two figures is the same. This proves that the determined angles are valid as they align with the spacecraft's movement, visualized on Figure 1 and are in the range of the camera's FoV. Their accuracy is elaborated in Section 4. The polar plot shows that the results of the angle determination in the camera frame yield results that are in the correct order of magnitude and line up with what can be seen in the images.

2.2. Transformation of Determined Line-of-Sight Vectors from Camera Frame to TOD

The observation angles determined from the images in Section 2.1 are defined in the camera frame and need to be transformed into the inertial True of Date (TOD) reference frame at the time of the observation. Therefore, the precise attitude and position of the observing spacecraft, in this case TUBIN, is required at the exact time of the observation.

The individual observation points are determined in Section 2.1 and are transformed as depicted in Figure 4.

The observation angles for every observation are transformed into a line-of-sight vector. This line-of-sight vector has an arbitrary length and points in the direction specified by the observation angles (azimuth and elevation). As a vector, it can easily be rotated using [5] to perform the necessary coordinate transformations.

Transformation is initiated by transforming the line-of-sight vector into the satellite body frame. For this, the mounting orientations including corrections from in-flight analysis determined for the TUBIN cameras in [6] are used.

Following, the line-of-sight vector is transformed into the TOD reference frame, accounting for the attitude of the spacecraft at the time of the observation. As the attitude is only available in discrete timestamps in the spacecraft's telemetry it needs to be interpolated to get the attitude at the time of observation. During this imaging campaign the attitude of TUBIN was recorded in $10\,\mathrm{s}$ intervals. As the spacecraft operated in active three-axis attitude control when the observations were taken, the attitude was almost constant from telemetry point to telemetry point. For timestamps in between two telemetry points the quaternions are interpolated using the Spherical Linear Interpolation of Rotations (Slerp) algorithm implemented in [5].

In addition to the observation vector, the precise position of the observing spacecraft at the time of the observation as made is required. The position of the spacecraft is taken from onboard global positioning system (GPS) measurements that area available directly in the TOD frame from the TUBIN spacecraft. Similar to the attitude, these are also only available at discrete timestamps, requiring interpolation. As the time between GPS positions is relatively short with $30\,\mathrm{s}$ a simple linear interpolation is used to reduce complexity. This introduces a mostly radial error in the position, that could be reduced by a more sophisticated interpolation approach.

To gauge the accuracy of the determined orbit, a ground truth state vector of the observed object is also needed at the time of the observation. For this purpose, the state vector of the observed object is derived from the TLE of the object valid at the time of the observations using the Skyfield Application Programming Interface (API) [7]. As the Skyfield API yields the state vector in the Geocentric Celestial Reference System (GCRS), it needs to be transformed into the TOD, correcting for precision and nutation at the time of the observation. This transformation is done using Orekit [8].

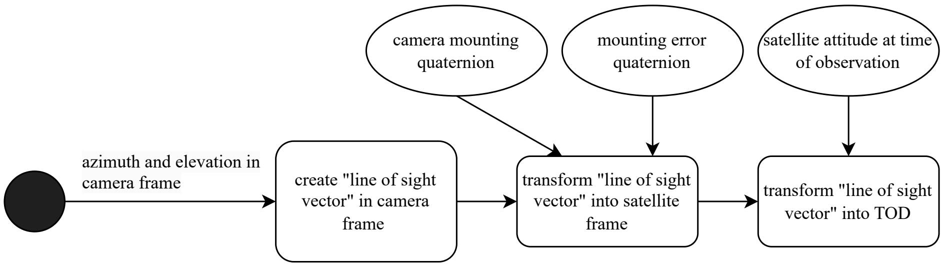

Figure 4. Coordinate Transformation from Camera Fixed Observation Angels, to TOD Line-of-Sight Vectors

3. ORBIT DETERMINATION WITH GAUSS-ANGLES-ONLY-APPROACH

As described in Section 1, this paper builds on a MATLAB code base developed by the involved students during the TU Berlin lecture "Space Mission Analysis". As this code base features an implementation of GAO as an IOD method. The existing GAO implementation was adapted to handle space-based observations instead of ground-based observations.

After the observation vectors have been extracted from the pictures using a Python script as described in Section 2, the orbit determination is performed in MATLAB using the GAO approach. In addition to the method description in Section 3.1, an analysis of the method itself and the resulting orbit is conducted in Section 3.2.

3.1. Method Description

The following data has been collected to get processed by the MATLAB script to determine the initial orbit using the GAO approach (also represented in Figure 5):

- n line-of-sight vectors from the detecting spacecraft to the detected spacecraft in ECI
- n positions of the detecting spacecraft in ECI
- n velocities of the detecting spacecraft in ECI
- n timestamps of the detecting spacecraft in UTC

The eight VIS images of this observation campaign result in $n = 16$ observation points as it is described in Section 2.1 that each image yields two observation points.

As discussed in Section 1, the goal of this paper is to gauge the accuracy and challenges when applying the IOD method GAO as described in [3] to space based observations. GAO requires exactly three chronological data points, available 16 data points are grouped into 560 groups. These groups represent all possible combinations to form a group of three data points in chronological order. TUBIN moves while capturing the images of ICEYE, constantly shifting the line-of-sight vector's origin. The GAO orbit determination method already includes this to compensate for the movement of the observing station due to, for example, the Earth's rotation. Therefore, the changing position of TUBIN can be taken into account for every data point. The accuracy of the position measurements and interpolation used is discussed in Section 4.

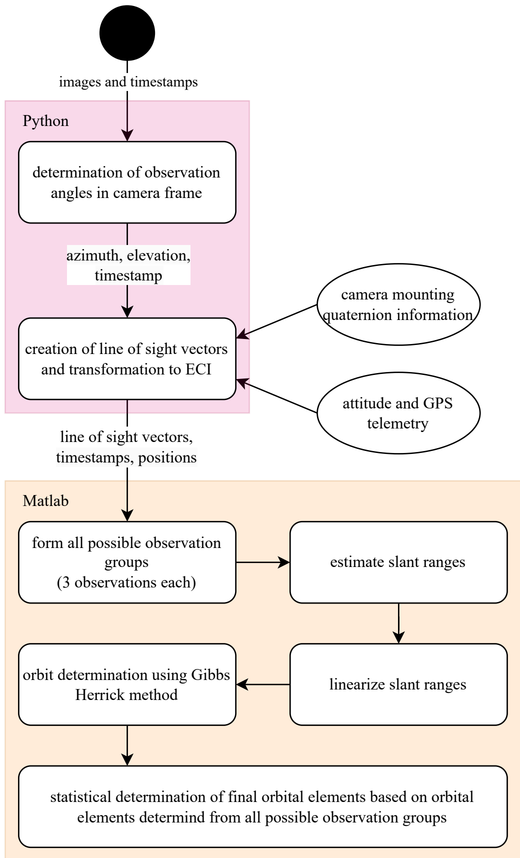

Figure 5. Flowchart of Orbit Determination Process from Images

The slant ranges between the passing spacecraft and the observing spacecraft of all three data points from each group are determined using GAO. With that, multiple slant ranges for each observation point are calculated. A range of filter techniques is employed to curb computational and statistical outliers. First, all negative slant ranges are eliminated. A linear fitting approach is applied to all positive slant ranges to further refine the slant ranges. This can be done by assuming that the slant ranges change linearly as a result of constant relative velocity during the short observation time. As a result, the refined slant range for each observation point is calculated using the linearization and the observation time.

For each of the 16 observation points, a slant range, a line-of-sight vector and the detecting spacecraft's position are determined. Subsequently, the slant range is multiplied by the line-of-sight vector and the detecting spacecraft's position is added. This results in an observation vector within the ECI coordinate system, assigned to a single observation point. Again, 560 groups of three are formed from the 16 observation vectors. Using the Gibbs and Herrick-Gibbs method, the velocity of the spacecraft at the middle observation points is defined respectively, obtaining 560 complete state vectors. In order to eliminate outliers due to data noise and inaccuracies, it is necessary to average all state vector components. Any state vector component below or above the mean plus or minus the standard deviation is neglected, which is called 1-sigma clipping. Finally, the remaining orbits/state vectors are averaged to obtain the final estimated orbit.

3.2. Analysis and Results

This section comprises an in-depth analysis of the results of the GAO method. Having 560 observation groups, each observation point is part of a group 105 times. However, not all slant ranges, belonging to the same observation point, are positive. Figure 6 shows how often the resulting slant range is negative and is therefore excluded when filtering the slant ranges. It can be seen that observation points 7 and 9 most frequently lead to negative slant ranges if they are part of a group, whereas 8 and 10 tend to lead to positive slant ranges. It can therefore be concluded that points 8 and 10 lead to usable results more frequently than when 7 and 9 are part of a group. Overall, 58.3 % of all groups result in a negative slant range.

A crucial part of the GAO method is the determination of the slant ranges. The resulting slant ranges are visualized in Figure 7. As explained in the method description in Section 3.1, the slant ranges are refined and linearly fitted, which is represented as the straight red line in Figure 7 resulting in a fixed slant range for each observation, depicted in Figure 8. The resulting state vectors based on the unrefined and refined slant ranges are presented in Figure 11 and Figure 14. It has to be mentioned that Figure 11 has fewer values because these states result from only the positive unrefined slant ranges and therefore 230 states remain. Comparing the consequent data, it can be

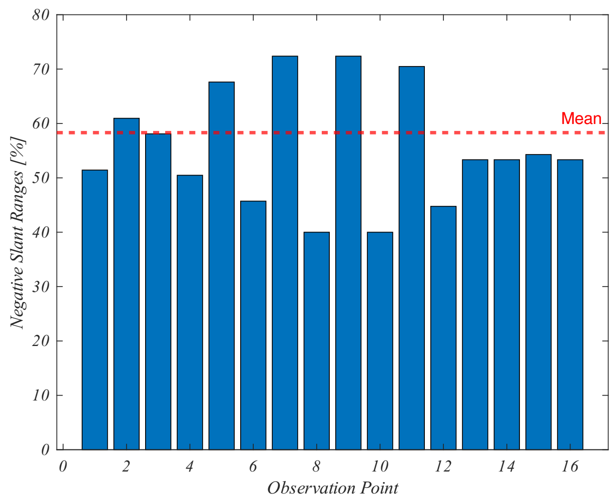

Figure 6. Percentage of negative slant ranges per observation point

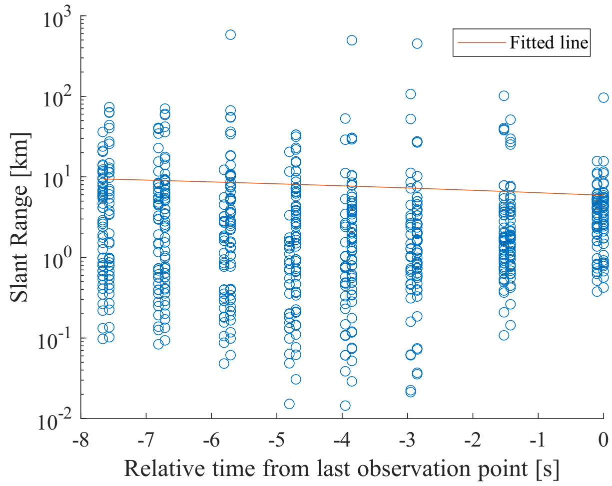

Figure 7. Positive Slant Ranges Resulting from All Observation Groups

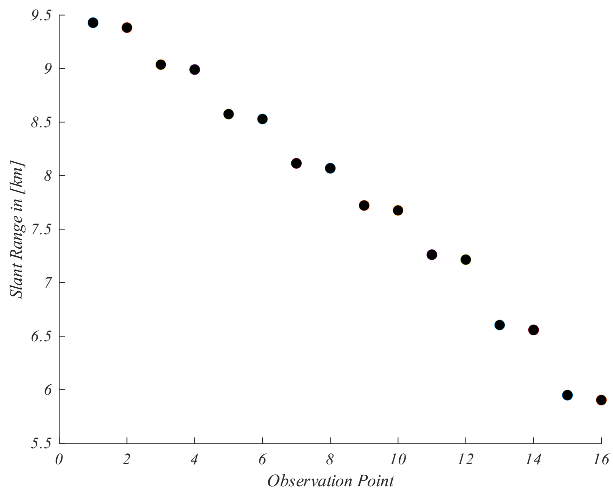

Figure 8. Fitted Slant Ranges of All 16 Observations

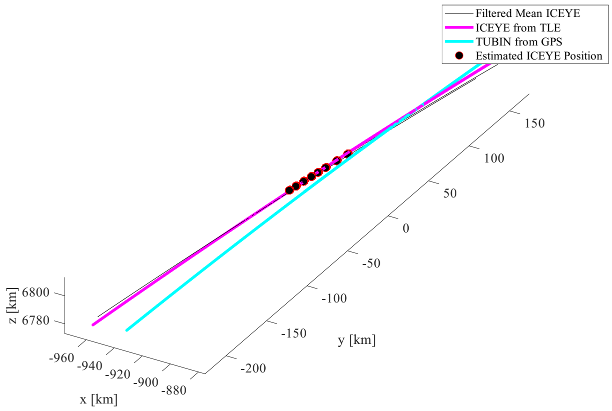

Figure 9. Observation Vectors of Positive and Refined Slant Ranges

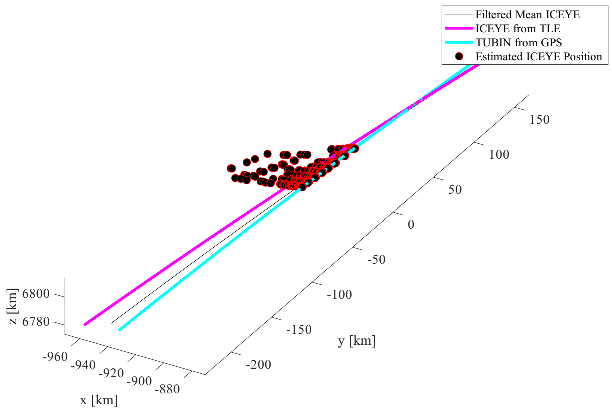

Figure 10. Observation Vectors of Positive and Unrefined Slant Ranges

seen that the state vectors calculated with only the positive and unrefined slant ranges in GAO have a lot more outliers than state vectors based on the filtered and refined slant ranges. This can be explained by the 16 fixed slant ranges used for all observation groups instead of unique ones calculated individually for each observation point, which provides a better final result.

The orbits propagated from these states are visualized in Figure 12 and Figure 15. Due to the large standard deviation of the state vector components based on the unrefined slant ranges, fewer outliers can be filtered as if refined slant ranges had been used, leading to a larger velocity offset from the targeted ICEYE state.

Table 1 encompasses the mean state vector elements (x, y, z, vx, vy, vz) of all 560 combinations based on refined and unrefined slant ranges and the mean state vectors of the remaining orbits after filtering/sigma clipping using the standard deviation. It can be seen that the *filtered mean orbit using unrefined slant ranges* has a higher velocity angle difference to the actual ICEYE orbit, other than the *unfiltered mean orbit using refined slant ranges*. On the other hand, the absolute position is more accurate. This gets clearer when looking at the visualization of these orbits in Figure 13 and Figure 16. It can be noticed that the orbit based on the unrefined slant ranges is very close to the own TUBIN orbit and the orbit resulting from the fitted slant ranges is closer to the ICEYE orbit. The Keplerian elements from these states can be seen in Table 1 as well. The semi-major axis (SMA) of the filtered state based on the refined slant ranges is off by about $250\,\mathrm{km}$ but the right ascension of the ascending node (RAAN) offset is reduced. The inclination (INC) is the same for all states, no matter which slant ranges are used. The orbits based on the fitted slant ranges have a more accurate RAAN but lack the SMA which is vice versa for the unfitted slant ranges. For the orbit based on the unrefined slant ranges, the own TUBIN orbit is likely determined and due to the similarity between the TUBIN and ICEYE orbit regarding the SMA is relatively accurate. Therefore, the final determined orbits based on the fitted slant ranges provide a better result and are plotted in Figure 16. In addition to the position and velocity differences, the angle offset is given. As mentioned before, the velocity direction is better when the refined slant ranges are used. The angle offset shows that filtering/clipping the state vector elements based on the mean and standard deviation reduces the result's accuracy. For better visualization, the best result is underlined in Table 1.

Figure 9 and Figure 10 show the estimated ICEYE position, based on the refined and unrefined slant ranges. As a reminder, the position is calculated by multiplying the line-of-sight vector with the slant range and adding the TUBIN position. The line-of-sight vectors and the TUBIN positions are the same for all observation points, so only the slant ranges are different in both figures. It can be seen that in Figure 10 (unrefined slant ranges) the estimated positions are widely spread, which is the major reason for the wrong orbits. The widely spread slant ranges used in this plot can be seen in Figure 7. For the refined slant ranges, the estimated ICEYE position is broadly accurate and does not vary much but here the inaccurate observation angles lead to a wrong SMA and eccentricity (ECC). The inaccurate observation angle or line-of-sight vector does not point to the ICEYE orbit propagated from the TLE. At the time of writing this paper, it is not clear why that is the case. The pointing error is described in more detail in Section 4.

Figure 14 shows the state vectors of the GAO approach with the refined slant ranges and Table 1 summarizes the mean state vectors and their Keplarian elements. These orbits are propagated for one revolution with respect to the actual TUBIN and ICEYE orbits. Figure 15 shows all 560 orbits as the result of using refined slant ranges for all observation groups. The final result of the GAO approach with only positive and refined slant ranges is shown in Figure 16.

In the Figures 12 and 13, the orbits resulting from unfitted but positive slant ranges are visualized. Figure 12 shows all determined orbits and it can be seen that there are a lot of outliers, which were already presented in Figure 11. The mean of the remaining orbits is therefore shown in

Table 1. Mean of State Vectors for Positive Slant Ranges and Difference to Actual ICEYE TLE State Vector - Un-/Filtered and Un-/Refined

State	Original ICEYE	Unfiltered/ Unrefined	Difference to ICEYE State	Filtered/ Unrefined	Difference to ICEYE State	Unfiltered/ Refined	Difference to ICEYE State	Filtered/ Refined	Difference to ICEYE State
x [km]	-927.18	-922.94	4.24	-919.82	7.36	-925.24	-13.88	-925.38	-14.02
y [km]	-36.51	-24.61	11.90	-24.73	11.78	-24.88	6.34	-25.90	5.32
z [km]	6792.54	6793.28	0.74	6793.45	0.91	6793.96	-1.74	6793.10	-1.60
Absolute Offset [km]			4.87		7.89		11.80		10.78
vx [km/s]	1.15	0.88	-0.27	0.68	-0.47	1.05	-0.14	1.05	-0.14
vy [km/s]	7.53	7.65	0.12	7.61	0.080	7.68	0.16	7.68	0.16
vz [km/s]	0.20	-0.074	-0.27	-0.039	-0.23	-0.04	-0.23	-0.09	-0.29
Absolute Offset [km/s]			0.39		0.53		0.30		0.34
Angle Offset [deg]			2.89		3.96		1.97		2.34
SMA [km]	6849.51	6997.88	148,37	6885.92	36,41	7096.81	247,3	7101.78	252,27
ECC []	0.00	0.34	0,34	0.021	0,021	0.04	0,04	0.05	0,05
INC [°]	97.63	97.66	0,03	97.66	0,03	97.66	0,03	97.66	0,03
RAAN [°]	261.13	263.49	2,36	264.94	3,81	262.28	1,15	262.32	1,19
AOP [°]	254.52	145.11	-109,41	168.18	-86,34	128.33	-126,19	135.17	-119,35
TAN [°]	193.99	303.81	109,82	280.93	86,94	320.43	126,44	313.58	119,59

Figure 13 and as expected from the Table 1.

In general, the analysis and results show that it is possible to determine a LEO even if the target orbit was not determined accurately. In contrast to the line-of-sight vectors, the slant ranges appear to have an accurate length. There is potential for the image-based angle determination to be improved, which is the basis of producing the line-of-sight vectors. With an advancement in the angle determination, the observation vectors could gain accuracy and therefore align with the detected spacecraft ICEYE's orbit. Furthermore, TUBIN's and ICEYE's orbits are quite similar, resulting in small deltas that are difficult to identify and uncertainties that weigh significantly more. Both spacecraft are situated within LEO with their RAAN exhibiting the most significant discrepancy.

It has to be mentioned that uncertainties in the TUBIN orbit also contribute to the difference between the estimated ICEYE orbit and its real one. Using the GAO approach in its original form, the ground station (G/S) is a fixed point on Earth's surface. Conversely, the adapted approach presented in this paper establishes a moving G/S.

4. ACCURACY AND ERROR ANALYSIS

The current implementation exhibits certain limitations, leaving room for further refinement. The accuracy of this method is subject to various sources of uncertainty, which may introduce errors in the results.

The exact absolute time reference of the images remains uncertain. The relative timing between images, as well as the duration from the start to the end of a single image acquisition is known with relatively high precision. However, the exact precision of the absolute time reference is not known as it is unknown with what precision the time was last set by the GPS receiver onboard TUBIN before or even during image acquisition. Additionally, time shifts caused by rolling shutters are not accounted for. This introduces an unknown small absolute time offset, potentially leading to deviations in the recorded timestamps. Consequently, these errors can affect the transformation from the camera frame to the ECI frame by introducing inaccuracies in the transformation process.

The attitude knowledge may also lead to inaccuracies in this part of the algorithm. This accuracy is determined by the sensors that are used on-board TUBIN. At the time of image acquisition, the star trackers of TUBIN have been enabled, which have an attitude determination accuracy of $0.1°$ [6]. Therefore, this accuracy needs to be taken into account when analyzing the results and searching for possible improvements to the method. Additionally, as stated in Section 2.2, attitude information is only available every $10\,\mathrm{s}$ during this campaign. However, from other imaging campaigns, it is known that there are higher frequency oscillations of the attitude of TUBIN. Therefore, the attitude determined by the Slerp interpolation is not the exact attitude at the time of the image capture. Therefore, more frequent recording of attitude telemetry is essential to improve attitude knowledge during future campaigns.

The position of TUBIN is interpolated linearly between the GPS measurement points. This linear interpolation is just an approximation of the real position at the time of image acquisition, which leads to errors in the transformation process. Also, there is an error in the position measurement itself. For TUBIN the single point solution is stated to be $10\,\mathrm{m}$ in position and $0.1\,\mathrm{m\,s^{-1}}$ in velocity in the datasheet [9].

The determination of the slant ranges is an essential part of the orbit determination. These may be calculated non-adequately with the GAO approach. An active instrument measuring the slant ranges like Light Detection and Ranging (LIDAR) or radar, or

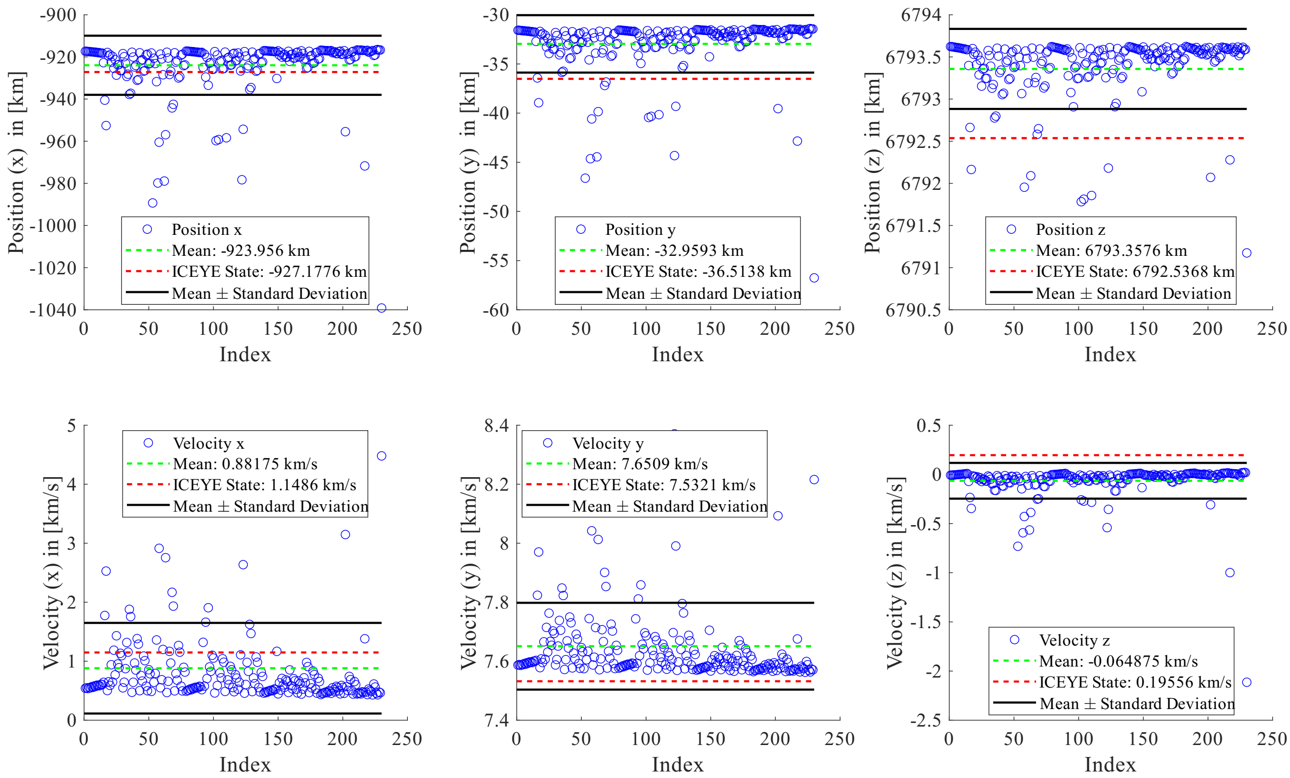

Figure 11. State Vectors Resulting from Unrefined Slant Ranges

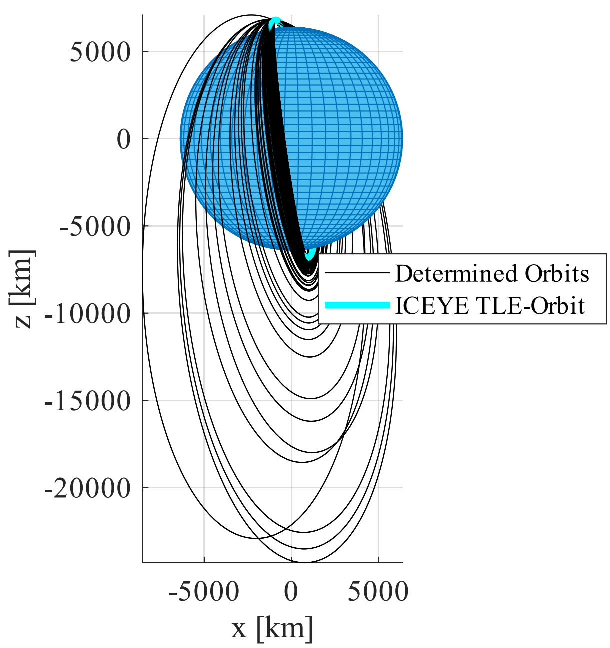

Figure 12. Determined Orbits of Unrefined Slant Ranges

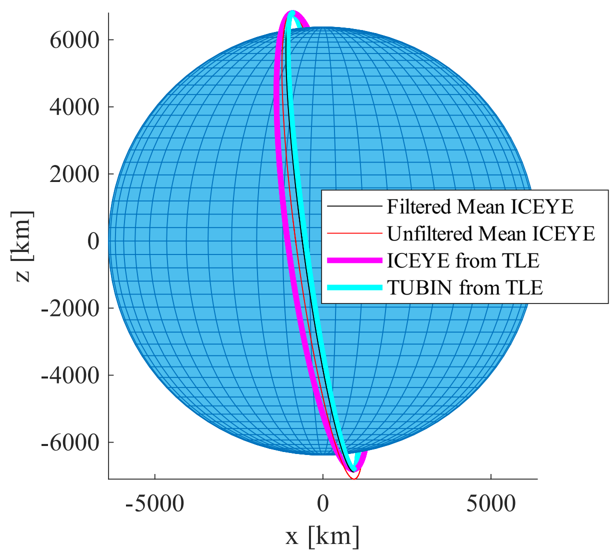

Figure 13. Final Determined ICEYE Orbit Using Unrefined Slant Ranges

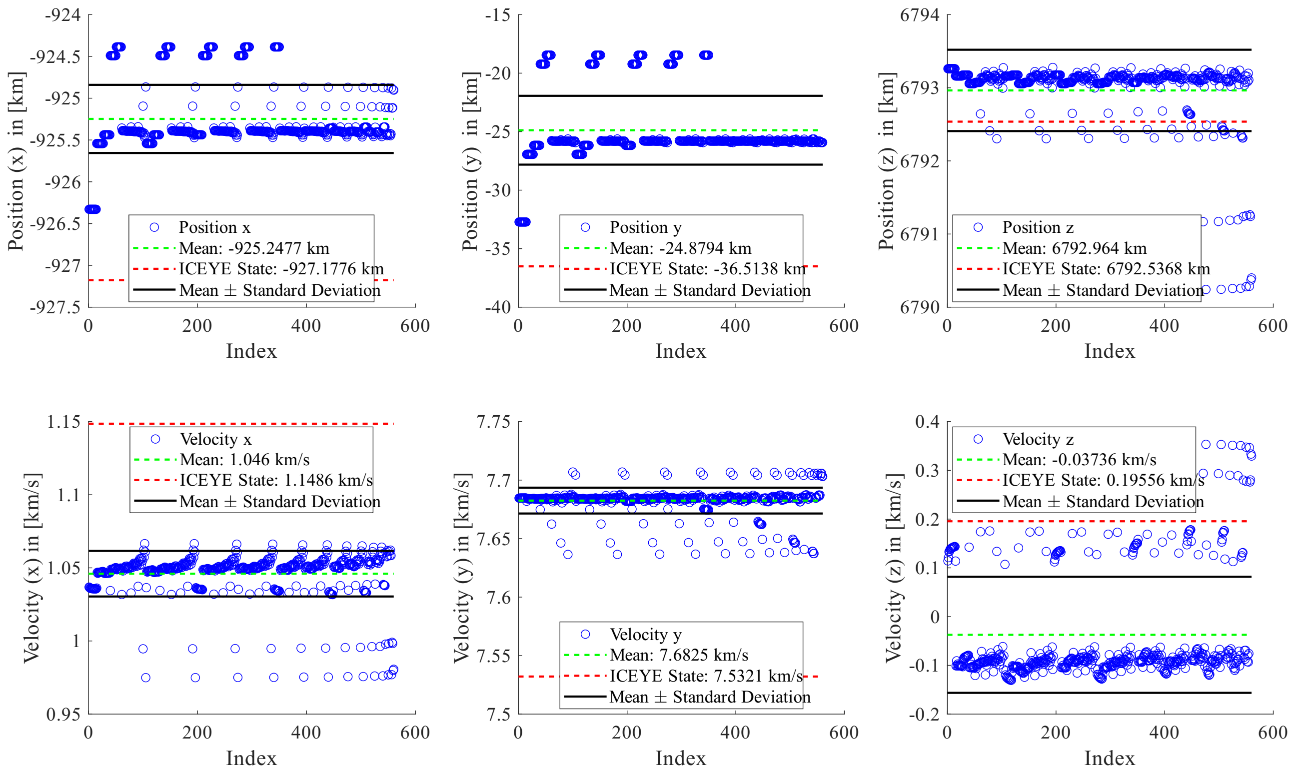

Figure 14. State Vectors Resulting from Refined Slant Ranges

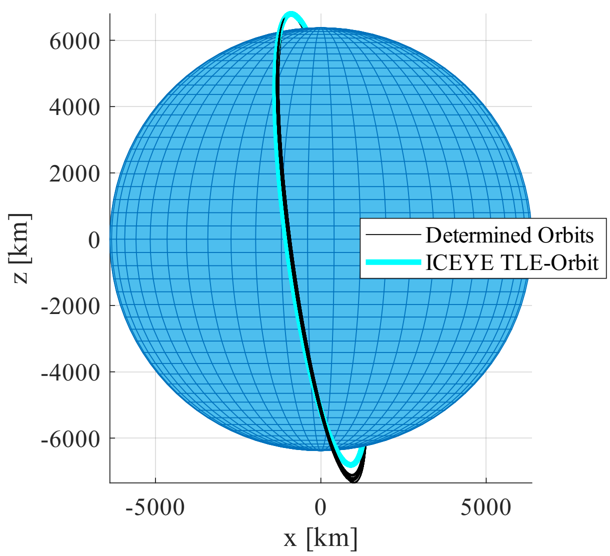

Figure 15. Determined Orbits of Refined Slant Ranges

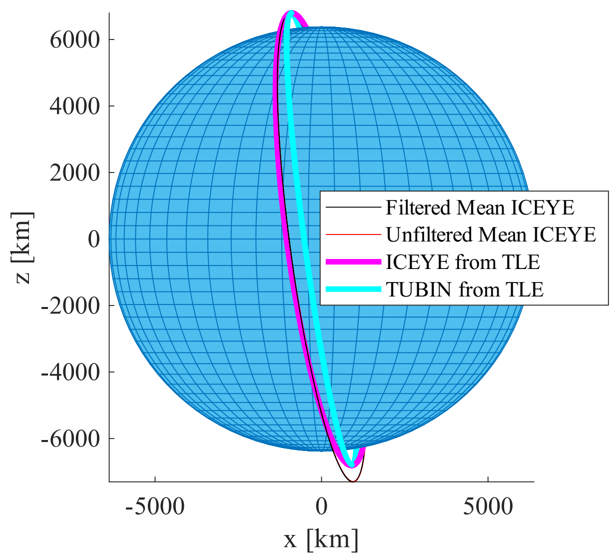

Figure 16. Final Determined ICEYE Orbit Using Refined Slant Ranges

stereoscopic imagery with a sufficiently large baseline could enable better results.

The currently used data set consists of eight images yielding 16 azimuth and elevation sets in the camera frame. A longer observation span over several orbits plays an important role in the improvement of the accuracy and this effect can already be seen when collecting data over more than two orbits [10]. Therefore, the small amount of data probably leads to high inaccuracies in orbit determination in the current process.

The used initial orbit determination method yields non-accurate results. Initially, Gauss solution was developed to determine orbits with ground-based observations [3]. In this work, the observations have been conducted in-space, misusing the methods algorithm. Also, the method works best with observation separation angles of $10°$ or less, which corresponds to observations with a maximum of five to ten minutes gap [3]. In this case, the observations are very close to each other, with gaps of less than a second. As this is orders of magnitude less than the mentioned $10°$, this potentially causes inaccuracies in the determined orbit. In comparison to other techniques like Gooding or Double r-iteration, Gauss solution may yield solutions with lower accuracy [3]. The results of 3.2 show these inaccuracies in the inadequate determination of the slant ranges and Keplerian elements, which do not fit the orbit that is given with the TLE.

The detection of a pixel may be false due to lightning conditions or a falsely set threshold for image processing. An analysis for false pixel detection is conducted as part of this work in Section 4.1.

4.1. Pixel Error Analysis

A pixel error analysis is conducted to analyze the error that results from an inaccurate recognition of the passing spacecraft's pixel position in the recorded images. In this analysis the influence of a single pixel offset in $\pm X$ or $\pm Y$ is investigated by calculating the change in direction of the resulting observation vector. For every pixel, the observation vector as well as the four possible observation vectors with a shift of one pixel in $+X$,$-X$,$+Y$, and $-Y$ are calculated. The resulting error in the observation vector is calculated as the angle between each of the observation vectors and the observation vector resulting from the original pixel. Figure 17 shows the maximum angular error in the observation vector resulting from a single pixel offset in $\pm X$ or $\pm Y$ for the Visual camera while Figure 18 shows the same analysis for the lower resolution infrared cameras. Additionally, the observation points of this particular campaign are depicted as detected in the respective camera frames. For both cameras, it can be seen that the error magnitude is fairly homogeneous, decreasing with distance from the center of the frame, at around $0.0041°$ for a single pixel offset on the VIS camera and around $0.026°$ for the IR cameras. For the VIS camera, which has a higher resolution than the IR cameras, this error is well below the minimum angle between two observed vectors which is $0.083°$. However, for the lower resolution infrared cameras, the value of $0.026°$ is in the same magnitude as the minimum angle between two observed vectors which is $0.033°$. This at least partially explains the less-than-ideal result when running the orbit determination algorithm only on the infrared images.

5. CONCLUSION

In conclusion, this work has shown the transferability between very basic IOD methods like GAO in combination with Gibbs and Herrick-Gibbs as frequently covered in orbital mechanics lectures with ground-based observations and space-based observations. Despite the very short observation time of only $8\,\mathrm{s}$ covering only a very small arc of the orbit, the resulting orbital elements are in the correct order of magnitude of the reference orbital elements of the TLE at the time. This study proves the usability and shows the benefits of using already existing space assets for early development of space situational awareness (SSA) technologies like space-based orbit determination. Simultaneously, this study identified some key design drivers to address in dedicated missions for studying SSA technologies like PRINCESS. The most critical features are high resolution, precise time as well as attitude knowledge as it allows for more precise determination of the observation vectors and thereby more precise orbit determination. Additionally, measurements from active instruments like LIDAR or radar could improve range determination, improving orbit determination. However, it is also important to state that this study is based on a limited number of observations taken during a single close encounter with low relative velocity. Additional encounters under more diverse conditions need to be analyzed to ensure the general validity of these results. Therefore, it is necessary to acquire additional datasets during upcoming close encounters to refine this tool chain before the TUBINs reentry in late 2025. Observations of objects on a diverse set of orbits in relation to the observing spacecraft could significantly contribute to further research in this manner. Furthermore, the orbit determination using the same images could be conducted with a sufficient method like the *Double-R Iteration* and the *Gooding method* [11],[12].

REFERENCES

[1] "Space safety, scanning and observing." (2025), [Online]. Available: `https://www.esa.int/Space_Safety/Space_Debris/Scanning_and_observing2` (visited on 03/24/2025) (cit. on p. 1).

[2] S. Grau, A. J. G. Siestrup, V. Koßack, *et al.*, "Precise in-orbit collision prediction and space environment surveillance system," in *The 4S Symposium*, Palma de Mallorca, Spain, 2024 (cit. on p. 1).

[3] D. A. Vallado, *Fundamentals of Astrodynamics and Applications - Fourth Edition*. Space Technology Library, 2013, pp. 433–499 (cit. on pp. 1, 4, 10).

[4] V. Koßack, T. Erdmann, and S. Grau, "Small satellite attitude verification using multispectral imagery of moon and earth horizon constellation," in *75th International Astronautical Congress*, Milan, Italy, 2024. DOI: 10.52202/078368-0019 (cit. on p. 2).

[5] P. Virtanen, R. Gommers, T. E. Oliphant, *et al.*, "SciPy 1.0: Fundamental Algorithms for Scientific Computing in Python," *Nature Methods*, vol. 17, pp. 261–272, 2020. DOI: 10.1038/s41592-019-0686-2 (cit. on p. 3).

[6] C. Jonglez, J. Bartholomäus, and P. Werner, "ADCS performance assessment using payload cameras: Lessons learned on the TechnoSat and TUBIN small satellite missions," in *14th IAA Symposium on Small Satellites for Earth System Observation*, Berlin, Germany, 2023 (cit. on pp. 3, 7).

[7] B. Rhodes, "Skyfield: High precision research-grade positions for planets and earth satellites generator," *Astrophysics Source Code Library*, ascl–1907, 2019 (cit. on p. 3).

[8] maisonobe, B. Cazabonne, E. Ward, *et al.*, *Cs-si/orekit: 12.2*, version 12.2, 2024-10. DOI: 10.5281/zenodo.13950582. [Online]. Available: https://doi.org/10.5281/zenodo.13950582 (cit. on p. 3).

[9] Deutsches Zentrum für Luft- und Raumfahrt e.V., "Phoenix - Spaceborne GPS Receiver", *Data Sheet*, 2007 (cit. on p. 7).

[10] J.-S. Ardaens and G. Gaias, "A numerical approach to the problem of angles-only initial relative orbit determination in low earth orbit," *Advances in Space Research*, vol. 63, no. 12, pp. 3884–3899, 2019 (cit. on p. 10).

[11] T. A. Henderson, D. Mortari, and J. Davis, "Modifications to the gooding algorithm for angles-only initial orbit determination," in *AAS/AIAA Space Flight Mechanics Meeting*, 2010 (cit. on p. 10).

[12] R. R. Karimi and D. Mortari, "Initial orbit determination using multiple observations," *Celestial Mechanics and Dynamical Astronomy*, vol. 109, pp. 167–180, 2011 (cit. on p. 10).

GLOSSARY

API Application Programming Interface. 3

ECC eccentricity. 6

ECI Earth-centered inertial. 2, 4, 5, 7

FoV field of view. 2, 3

G/S ground station. 7

GAO Gauss Angles-Only. 1, 2, 4–7, 10

GCRS Geocentric Celestial Reference System. 3

GPS global positioning system. 3, 7

ICEYE ICEYE-12. 1, 4, 6–9

INC inclination. 6

IOD Initial Orbit Determination. 1, 4, 10

IR Infra-Red. 1, 2, 10

LEO Low Earth Orbit. 1, 7

LIDAR Light Detection and Ranging. 7, 10

MEHthod Moon and Earth Horizon Method. 2

PRINCESS PRecise IN-orbit Collision prediction and space Environment Surveillance System. 1, 2, 10

RAAN right ascension of the ascending node. 6, 7

Slerp Spherical Linear Interpolation of Rotations. 3, 7

SMA semi-major axis. 6

SSA space situational awareness. 10

TLE two-line element. 2, 3, 6, 10

TOD True of Date. 3, 4

TU Berlin Technische Universität Berlin. 1, 4

TUBIN Technische Universität Berlin Infrared Nanosatellite. 1–4, 6, 7, 10

UTC Coordinated universal time. 4

VIS visible spectrum. 1, 2, 4, 10

APPENDIX

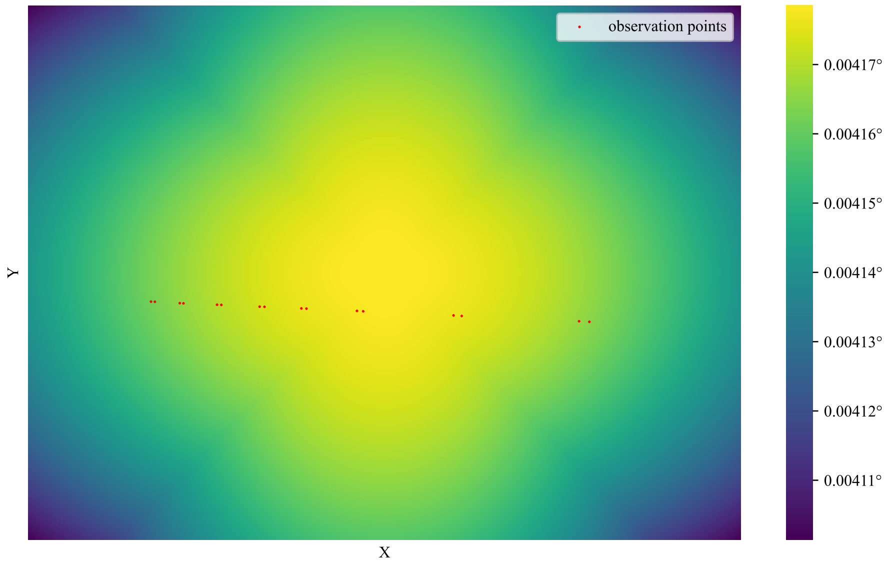

Figure 17. Visual Camera Maximum Error in Observation Vector Direction Resulting from Single Pixel Shift in ($\pm X$ or $\pm Y$)

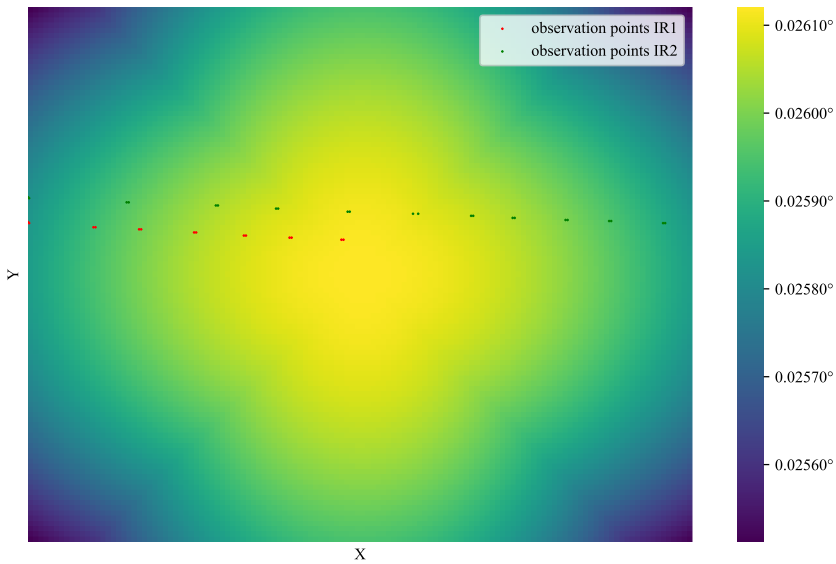

Figure 18. Infrared Cameras Maximum Error in Observation Vector Direction Resulting from Single Pixel Shift in ($\pm X$ or $\pm Y$)